



# Enhancing the spatio-temporal features of polar mesosphere summer echoes using coherent MIMO and radar imaging at MAARSY

Juan Miguel Urco<sup>1</sup>, Jorge Luis Chau<sup>1</sup>, Tobias Weber<sup>2</sup>, and Ralph Lateck<sup>1</sup>

<sup>1</sup>Leibniz Institute of Atmospheric Physics at the University of Rostock, Germany

<sup>2</sup>University of Rostock, Germany

**Correspondence:** J.M. Urco ([urco@iap-kborn.de](mailto:urco@iap-kborn.de))

**Abstract.** Polar mesospheric summer echoes (PMSEs) are very strong radar echoes caused by the presence of ice particles, turbulence, and free electrons in the mesosphere over polar regions. For more than three decades, PMSEs have been used as natural tracers of the complicated atmospheric dynamics of this region. Neutral winds and turbulence parameters have been obtained assuming PMSE horizontal homogeneity in scales of tens of kilometers. Recent radar imaging studies have shown that PMSEs are not homogeneous in these scales and instead they are composed of kilometer-scale structures. In this paper, we present a technique that allows PMSE observations with unprecedented angular resolution ( $\sim 0.6^\circ$ ). The technique combines the concept of coherent MIMO (Multi-input multiple-output) and two high-resolution imaging techniques, i.e., Capon and Maximum Entropy (MaxEnt). The resulting resolution is evaluated by imaging specular meteor echoes. The gain in angular resolution compared to previous approaches using SIMO (single-input and multiple-output) and Capon is at least a factor of 2, i.e., at 85 km, we obtain a horizontal resolution of  $\sim 900$  meters. The goodness of the new technique is evaluated with two events of three-dimensional PMSE structures showing: (1) horizontal wavelengths of 8-10 km and periods of 4-7 minutes, drifting with the background wind, and (2) horizontal wavelengths of 12-16 km and periods of 15-20 minutes not drifting with the background wind. Besides the advantages of the implemented technique, we discuss its current challenges, like the use of reduced power-aperture and processing time, as well as the future opportunities for improving the understanding of the complex small-scale atmospheric dynamics behind PMSEs.

*Copyright statement.* TEXT

## 1 Introduction

The so called MIMO (Multiple Input Multiple Output) technique is being widely used in the fields of telecommunications and radar remote sensing (e.g Telatar, 1999; Huang et al., 2011; Foschini and Gans, 1998). Recently Urco et al. (2018) have shown that the use of multiple-transmitters and multiple-receivers can significantly improve the angular resolution of coherent atmospheric/ionospheric radars. In that work, MIMO was used to observe equatorial electrojet (EEJ) field-aligned irregularities



at Jicamarca in combination with the well-established radar imaging technique Capon (e.g., Palmer et al., 1998). The multiple transmitter part was implemented with three different diversity schemes, i.e., temporal, code, and polarization. The resulting angular resolution was superior, at least a factor of 4 to previous efforts using a single transmitter and the same receiving configuration, i.e., SIMO. Given that the EEJ irregularities are field-aligned with the Earth's magnetic field, angular imaging was performed only in the magnetically East-West direction.

Based on this successful implementation, we decided to implement coherent MIMO to improve the angular resolution of the Middle Atmosphere ALOMAR Radar System (MAARSY) (16.04°E, 69.30°N) and to study polar mesospheric summer echoes (PMSEs). PMSEs present strong radar cross sections (RCSs) that allow observing them with less transmitting power, which is the case when using MIMO. Previous efforts to study their spatial structure have been limited to a few kilometers spatial and a few minutes temporal resolutions (e.g., Yu et al., 2001; Latteck et al., 2012a; Stober et al., 2013; Sommer and Chau, 2016). Recently, Stober et al. (2018) has presented many examples of monochromatic gravity waves (GWs) and Kelvin-Helmholtz instabilities (KHIs) using nine days of multi-beam PMSE observations with MAARSY.

PMSEs are strong echoes, more than 50 dB stronger than expected echoes from free electrons in the D region, and there is a consensus that they are generated by atmospheric turbulence and require the presence of free electrons and charged ice particles (e.g., Rapp et al., 2002; Varney et al., 2011, and references therein). Although PMSEs have been studied since the late 1970s (e.g., Ecklund and Balsley, 1981; Hoppe et al., 1988; Kelley and Ulwick, 1988; Havnes et al., 1996; Rapp and Lübken, 2004), until recently they have been considered very aspect sensitive and homogeneous in scales of a few tens of kilometers at least when observed at very high frequencies (VHF) (e.g. Czechowsky et al., 1988; Zecha et al., 2001; Yu et al., 2001).

Based on recent multi-beam observations as well as radar imaging, Sommer and Chau (2016) have concluded that the PMSEs are not as aspect sensitive as previously reported, and instead, they are most of the time organized in kilometer-scale spatial structures drifting across the observing beams. Such results have been independently verified with bistatic observations at VHF, where PMSEs were observed with small systems at zenith angles close to 30° (e.g., Chau et al., 2018).

The results of Sommer and Chau (2016) were obtained with MAARSY using the whole antenna array for transmitting and an antenna compression approach, i.e., a wide beam by properly phasing the antennas (e.g., Woodman and Chau, 2001), and a multiple-receiver configuration. The spatial structures were obtained with the Capon technique due to its implementation simplicity and its relatively fast processing speed.

Given that PMSEs are highly associated to Noctilucent clouds (NLCs) (e.g., Hoppe et al., 1990; Stebel et al., 2000; Kaifler et al., 2011), spatial structures ranging from a few hundreds of meters to a few tens of kilometers observed in NLCs (e.g., Baumgarten and Fritts, 2014) are expected to be observed also in PMSEs. Indeed this is the case, PMSE structures of a few kilometers have been already reported by Sommer and Chau (2016) and structures of a few tens of kilometers have been reported by Chau et al. (2018).

Although progress has been made in discriminating between spatial and temporal ambiguities in PMSE observations, the achieved angular resolution has been mainly limited by two factors: (1) the effective area in the visibility plane, and (2) the number of independent spatial samples (e.g., Woodman, 1997). By implementing MIMO, we are able to improve both, i.e., a larger effective area, and a higher number of independent visibility samples. In addition, by implementing Maximum Entropy



(MaxEnt) which is more computationally demanding than Capon, we are able to further improve the angular resolution (e.g., Hysell and Chau, 2006). In this work, we have implemented coherent MIMO using three spatially separated transmitter sections and time diversity at MAARSY. On reception, we have used 15 separate receivers and the effective number of virtual receivers by using MIMO was 45. The resulting angular resolution was  $\sim 0.6^\circ$ , i.e., equivalent to a visibility area of 450 m diameter, more than 5 times larger than the nominal diameter of the MAARSY antenna.

Our paper is organized as follows. We first present the experiment configuration with a specific emphasis on the MIMO implementation. Then we describe the radar imaging implementation for both Capon and MaxEnt techniques. The PMSE results are shown in Section 4 for SIMO and MIMO using both Capon and MaxEnt. Within this section, two events are studied in detail, one where the observed waves drift with the background wind, and a second one where the waves do not propagate with the wind. Finally, the results of our MIMO implementation are discussed followed by conclusions.

## 2 Experiment configuration

### 2.1 MAARSY

MAARSY is an active phased antenna array operating at 53 MHz located in Andoya, Norway ( $69.30^\circ N, 16.04^\circ E$ ). The array consists of 433 antenna elements, each with its own transceiver module that allow us to modulate the antennas in phase and amplitude independently. Using this capability the transmitting or receiving beam can be steered in a desired direction up to  $30^\circ$  off zenith with an angular resolution of  $3.6^\circ$  (Latteck et al., 2012a, e.g., see ). In addition to its multibeam capability, MAARSY can be used for in-beam imaging experiments. In this case, the signals from a selected number of receiving antennas are stored and later a digital beamforming algorithm (imaging) is applied to the data. Unlike the multi-beam experiment, imaging allows obtaining a 2D image at once, avoiding the interleave from beam to beam. Currently, only 16 receivers are available at MAARSY. These 16 receive signals can be selected from groups of 7 antennas each called "hexagons" or from a group of 7 hexagons called "anemones" (e.g., see Latteck et al., 2012b, for further technical details). For this campaign, we conducted an imaging experiment using 15 hexagons on reception similar to Sommer and Chau (2016)'s experiment. One receiver is always connected to the full antenna array and it is used as in the standard multiple experiments. The radar parameters of this experiment are summarized in Table 1.

### 2.2 MAARSY MIMO configuration

In order to improve the performance of our imaging experiment, we applied a coherent MIMO technique [Urco et al. (2018)]. The technique employs multiple independent transmitting antennas and multiple receiving antennas, both spatially separated, to take advantage of the transmit-receive geometry and to increase the angular resolution of the radar. If the antennas are closely separated or collocated, the signals from each transmitting-receiving path are coherent and can be combined to form a larger virtual receiving array. The resulting number of virtual receivers is equal to the number of transmitters times the number of receivers.



Depending on the transmitting and receiving antenna configuration some virtual receivers can be redundant. In our experiment, we carefully selected the transmitting and receiving antenna configuration to get 3 special redundant virtual receivers. These 3 redundant virtual receivers were used for phase calibration of the transmitters as it was done by Urco et al. (2018). Figure 1a shows the 15 hexagons used in reception and the 3 anemones used in transmission (B, D, F). Figure 1d shows the resulting virtual receiving antennas where 3 of them are redundant and located at the origin.

In order to separate the contribution of each transmitter a form of transmit diversity was needed. In Urco et al. (2018), 3 types of transmit diversity were proposed: Code, time and polarization. Code diversity is recommended for atmospheric observations given that this is not sensitive to the temporal correlation or polarization of the target of interest. Unfortunately, code diversity cannot be currently used in MAARSY. For targets where the temporal correlation is less than the time separation between transmitters, time diversity can be applied. Given that PMSEs have a relative long correlation time (a few hundreds of milliseconds) we applied time diversity to enhance the spatio-temporal features of PMSE. The effective time separation between transmitters was 4, 4, 8 milliseconds between pairs BD, DF, and BF, respectively.

As explained by (Urco et al., 2018), in a monostatic coherent MIMO radar the relationship between the normalized spatial cross-correlation of signals from two different transmitting-receiving paths and the angular distribution of scattered power for a given range and frequency bin can be described by:

$$\frac{\langle v_{mp} * v_{nq}^* \rangle}{\sqrt{\langle |v_{mp}|^2 \rangle \langle |v_{nq}|^2 \rangle}} = V(\mathbf{k}(\Delta \mathbf{r}_{mn} + \Delta \mathbf{r}_{pq})) \quad (1)$$

$$= e^{(j2\pi f_d \tau + \phi_{mn} + \phi_{pq})} \cdot \int B(\theta) \cdot e^{-j\mathbf{k}(\Delta \mathbf{r}_{mn} + \Delta \mathbf{r}_{pq})} d\theta, \quad (2)$$

where:  $v_{mp}$  is the signal from the transmitting-receiving path  $(m, p)$ , being  $m$  the receiver and  $p$  the transmitter;  $v_{nq}^*$  is the complex conjugate of the signal from the transmitting-receiving path  $(n, q)$ , being  $n$  the receiver and  $q$  the transmitter;  $\langle v_{mp} * v_{nq}^* \rangle$  is the cross-correlation of two signals from antennas spatially separated;  $V(\mathbf{k}(\Delta \mathbf{r}_{mn} + \Delta \mathbf{r}_{pq}))$  is the visibility sample at  $(\Delta \mathbf{r}_{mn} + \Delta \mathbf{r}_{pq})$ ;  $\mathbf{k}$  is the wave number vector equal to  $(2\pi/\lambda)\theta$ . And  $\lambda$  is the radar wavelength;  $\theta$  is the angle of arrival equal to  $(\theta_x, \theta_y, \theta_z)$  which are the direction cosines in the  $(x, y, z)$  direction;  $B(\theta)$  is the angular scattered power distribution, also known as brightness;  $\Delta \mathbf{r}_{mn}$  is the spatial separation between receivers  $m$  and  $n$ ;  $\Delta \mathbf{r}_{pq}$  is the spatial separation between transmitters  $p$  and  $q$ ;  $2\pi f_d \tau$  is the phase difference due to the Doppler shift of the target,  $f_d$ , and  $\tau$  is the time separation between transmitters;  $\phi_{pq}$  is the phase difference between transmitters;  $\phi_{mn}$  is the phase difference between receivers.

A quick comparison between the visibility (sampling domain) for SIMO and MIMO shown in Figs. 1b and 1e, indicates that the antenna aperture for MIMO is larger than the SIMO by  $\sim 50\%$ . The difference lies in that the MIMO antenna aperture is defined as the maximum separation between two virtual receiving antennas, i. e.,  $\text{Max}(\Delta \mathbf{r}_{mn} + \Delta \mathbf{r}_{pq})$ . Whereas for SIMO  $\Delta \mathbf{r}_{pq} = 0$  and the antenna aperture is only defined by the maximum spatial separation between two receiving antennas. Figures 1c and 1f show the resulting instrument function or point spread function for SIMO and MIMO, respectively. As expected the half-power beam-width (HPBW) for MIMO is  $\sim 50\%$  smaller than for SIMO resulting in an angular resolution of  $2.4^\circ$  for MIMO compared to  $3.6^\circ$  for SIMO. Furthermore, the sidelobes in the MIMO configuration are strongly reduced given that the visibility is larger and contains no gaps.



### 3 Radar imaging implementation

Before inverting Eq. 2, the three phase differences due to time diversity ( $2\pi f_d \tau$ ), to receivers ( $\phi_{mn}$ ), and to transmitters ( $\phi_{pq}$ ) need to be corrected. When the analysis is done in frequency domain we can easily correct the value  $2\pi f_d \tau$  given that we know the frequency and the time separation between transmitters. On the other hand, the phase offsets between receivers have  
 5 been calibrated using Cassiopeia A as a radio source (e.g., Chau et al., 2014). Additionally, we have calibrated the phase offset between transmitters using the 3 redundant virtual receivers described above. Each of the redundant virtual receivers comes from one transmitter. They were compared to have zero phase difference between each other, given that they three must be located at the same virtual position (see, e.g., Urco et al., 2018, for more details).

Once the imaging system is calibrated we can invert Eq. 2 to obtain the estimated brightness  $B(\hat{\theta})$ . Given that the number  
 10 M of unique visibility samples is still less than the number N of unknowns (Brightness points) some kind of regularization is needed to solve Eq. 2. Two of the most well known radar imaging techniques applied to atmospheric/ionospheric targets are Capon (Palmer et al., 1998) and MaxEnt (Hysell, 1996).

#### 3.1 Capon technique

As described by Kudeki and Sürücü (1991), the angular resolution obtained from a direct inversion of Eq. 2 using the inverse  
 15 Fourier transform is limited by the longest baseline and the unmeasured antenna separations (visibility gaps). Palmer et al. (1998) proposed a new technique to improve the angular resolution based on the work of Capon (1969). Capon can be seen as an extension of the Fourier inverse transform. The difference lies in the fact that Capon chooses the antenna weights adaptively in order to minimize the sidelobe interference from signals outside of the direction of interest according to the data. Capon's technique provides an estimate of the brightness function given by:

$$20 \quad B(\hat{\theta}) = \frac{1}{M^H \cdot V^{-1} \cdot M}, \quad (3)$$

where  $M = [e^{-jk(r_{m_0} + r_{p_0})}, e^{-jk(r_{m_0} + r_{p_1})}, \dots, e^{-jk(r_{m_1} + r_{p_0})}, \dots]^T$  is the Fourier kernel and  $V = V\{k(\Delta r_{m_i m_j} + \Delta r_{p_k p_l})\}$  is the visibility due to the virtual receivers  $v_{m_i p_k}$  and  $v_{m_j p_l}$ , with i and j being the receiver indices and l and k being the transmitter indices.

#### 3.2 Maximum Entropy technique

25 Even when MIMO is used, the problem is still underdetermined. Thus, there are infinite possible image solutions, B, which agree with the data, V. Of all possibilities, MaxEnt chooses the solution with the maximum entropy or minimal information content (e.g., Hysell, 1996), as the one to be the most likely brightness distribution and the most consistent with the available visibility data and their statistical uncertainties. The entropy for a given frequency bin and range can be defined as:



$$S = \sum_{\theta} B(\hat{\theta}) \ln B(\hat{\theta}) / F \quad (4)$$

$$F = \sum_{\theta} B(\hat{\theta}) \quad (5)$$

where  $F$  is the summation of the brightness distribution over the region of interest. The solution of Eq. 2 is defined by:

$$\max_{\theta} \{S\} \quad \text{subject to} \quad |V - M \cdot B(\hat{\theta})| < \epsilon \quad (6)$$

- 5 where  $\epsilon$  is the noise amplitude associated with the visibility measurements. In this work, we have also considered the improvements of Hysell and Chau (2006). Specifically, we have taken into account the transmitting beam pattern and the statistical uncertainties of all the visibility pairs.

## 4 Results

Figure 2 shows the resulting 24-bit Range-Time-Doppler-Intensity (RTDI) image of the vertical beam for 32 hours of continuous operation on July 16 and 17, 2017. This plot was obtained after applying MaxEnt to the data and selecting the values that belong to the zenith angle. The signal intensity is represented as lightness, Doppler information as hue, and spectral width as saturation. As shown later, the resulting HPBW for this experiment is  $<1^\circ$  indicating that the Doppler information must be mainly due to the vertical motion. The RTDI plot indicates that the vertical motion is slow (green color) as expected. Nevertheless, there are two regions at 23:30LT and 06:30LT around 89km where the Doppler velocity present unrealistic values. Indeed, 15 PMSE were too strong at that time so that even the antenna sidelobes can be seen. Unfortunately, the imaging algorithm cannot assign the correct angle of arrival to these unusually strong echoes due to the angular ambiguity associated to our antenna array. The angular ambiguity is defined by the minimum separation between two antennas. The smaller the separation the larger the angle without ambiguity (e.g., Woodman, 1997). A manual angular correction can be applied knowing the Doppler but it is a hard task in the presence of many targets. A smaller baseline is recommended in future experiments for these special cases.

### 20 4.1 SIMO vs MIMO Results

Since the estimated brightness is expressed in polar coordinates,  $(\theta_x, \theta_y, R)$ , a cubic spline interpolation was applied to convert them to Cartesian coordinates,  $B(\theta_x, \theta_y, R)$  to  $B(x, y, z)$ , with the radar being located at the center ( $x=0, y=0, z=0$ ). Below we show the results of two selected events (Event 1 and Event 2) after performing such interpolation. For both events, we show  $x$  vs  $y$  cuts for a given  $z$ , as well as  $x$  vs  $z$  cuts for a given  $y$ . Where  $x$ ,  $y$ , and  $z$  represent the East-West (EW) direction, North-South 25 direction (NS) and Altitude, respectively.

Examples of EW-NS and EW-Altitude 2D images for Event 1 obtained by applying Capon and MaxEnt to two different antenna configurations, SIMO and MIMO, are shown in Figs. 3 and 4, respectively. Four different results are shown (a) SIMO-Capon, (b) SIMO-MaxEnt, (c) MIMO-Capon, and (d) MIMO-MaxEnt. As expected, MIMO shows a cleaner and more defined



image compared to SIMO, when either Capon or MaxEnt is used. However, we notice a great improvement for MIMO-MaxEnt as compared to SIMO-MaxEnt which it is not as clear in the case of MIMO-Capon vs SIMO-Capon. This improvement results from the fact that Capon tries to reduce the side-lobes adaptively steering the sidelobes to echo-free zones. Unfortunately, in this case, most of the illuminated area is filled with PMSE scattering and thus the performance of Capon is poor. Later we show an example of a point-like target to demonstrate that under certain conditions MIMO-Capon is better than SIMO-MaxEnt. Coming back to our comparison SIMO vs MIMO, with MIMO-MaxEnt small wave-like structures of 2 km wavelength can be clearly observed, which are invisible in SIMO implementations or MIMO-Capon. For example, observe the two wavefronts at  $x=10$  km in Fig. 3d, right beside the larger wave of 6 km wavelength. It indicates that waves-like structures of different wavelengths coexist within PMSE as previously seen in NLC (e.g., Baumgarten and Fritts, 2014). In addition, Fig. 4d shows that the ascending targets (red color) have higher SNR than the descending targets (blue color).

We show similar 2D cuts for Event 2, in Figs. 5 and 6 for  $z=82.7$  km and  $y=-6$  km, respectively. In this case, the observed wavelength is 12 km. Unlike the first event, the SNR is similar for targets with negative and positive Doppler. Figure 6d shows two very interesting points: (a) a very well defined wave-like structure between 82-84 km and (b) a quasi-uniform structure between 84-86 km which apparently has been modulated by the first wave. In this case, the wave-like structure is easily discernible even with SIMO-Capon, given that the wavelengths are larger than in Event 1 (see Fig. 5a).

## 4.2 MIMO results

Having shown the better qualitative performance of MIMO-MaxEnt with respect to the other three implementations for the two selected events above, next we present extended results using just MIMO-MaxEnt.

Figure 7 shows the evolution in time of two selected events, i.e., Event 1 (left), and Event 2 (right). Figures 7a and 7d show the Altitude vs time evolution for selected EW and NS coordinates. In these plots, we can appreciate how variable PMSE structures are, showing different altitudinal extensions. Note that the effective horizontal area is less than  $1 \text{ km}^2$  in both cases.

In the EW and NS keograms (second and third row of Fig. 7 respectively), we included the zonal ( $u_0$ ) and meridional ( $v_0$ ) wind velocity estimated from combining a couple of specular meteor radars (SMRs) (pink arrow) and from MAARSY based on PMSE Doppler velocities (yellow arrow). The arrow slope in the figure indicates the magnitude of the wind. The SMR winds were obtained from combining SMR detections from Andenes and Tromso in northern Norway (e.g., Chau et al., 2017, for details). In order to estimate the winds from PMSE we used the following formula:

$$v_{rad}(\theta_x, \theta_y, \theta_z) = u \cdot \theta_x + v \cdot \theta_y + w \cdot \theta_z \quad (7)$$

where  $v_{rad}$  is the radial wind,  $(\theta_x, \theta_y, \theta_z)$  are the direction cosines and  $(u, v, w)$  are the zonal, meridional and vertical wind direction, respectively. Assuming a constant  $u, v$ , and  $w$  for a given altitude bin and time bin, and taking all the measurements with SNR higher than -5dB we can invert Eq. 7 and get  $u_0, v_0$  and  $w_0$ , mean values of  $u, v$  and  $w$  respectively.

Analyzing the keograms for Event 1, i.e., from 00:50 to 01:05 UTC in Fig. 7a, we observe that the wave-like structure is very stable and it keeps its amplitude in the  $z$ -direction. In the EW direction, see Fig. 7b, this wave drift with the background wind



and might be an indication of a KHI event. Given that the wave is parallel to the NS direction, figure 7c shows the front waves each time they cross the beam. The meridional velocity indicates that the wave must travel from South to North at 20 m/s. Apparently, this horizontal wave stays parallel to the NS direction, however, it is also traveling in the NS direction with the background. Looking carefully at the first front wave reaches  $y=6$  km, the second one reaches  $y=10$  km and the last one a bit more. Unfortunately, our limited illuminated area width does not allow us to corroborate it.

Figure 7d shows another interesting wave example (Event 2). Unlike the first case, this wave does not keep its amplitude in  $z$ . It grows and then breaks. Its direction of propagation in  $x$  and  $y$  is even more interesting. As shown in Fig. 7e, the direction of propagation in the EW direction is completely opposite to the background wind. Whereas the wind is going from East to West, the wave propagates from West to East. In the NS direction, the wind is close to zero and we do not expect changes in this direction.

PMSE has been used as a neutral wind tracer assuming that  $u$ ,  $v$  and  $w$  are constant and homogeneous during the analyzed time (e.g., Balsley and Riddle, 1984; Fritts et al., 1990; Hoppe and Fritts, 1995; Stober et al., 2013). Therefore, those works assumed that scatters from PMSE are moving with the neutral wind at the same velocity and in the same direction. Unlike winds obtained from SMR, winds from PMSE are affected by local disturbances as shown in Figs. 7e and 7f. When the dynamics of local structures are not in agreement with the wind dynamics a bias could be introduced in the wind estimation (as shown in the Event 2). However, when these local disturbances are moving with the wind the estimated wind is not affected (Event 1). Note that the PMSE winds are in good agreement with the SMR winds in Event 1, but they are not for Event 2, particularly for the meridional component.

An animated sequence of the two events have been included as supplemental material, i.e., Movie S1 and S2. For both events, the sequence includes selected cuts of EW-NS, EW-Altitude, and NS-Altitude. In the Movie S1, we identify at least four examples of monochromatic waves with different wavelengths drifting with the wind in the direction North-West (at 23:57:37, 00:02:24, 00:10:57, 00:55:33 UTC). Interestingly in this case, longitudinal and transverse waves both drift with the background wind. In Movie S2, we show the complete evolution in time of Event 2. In the EW-Altitude cut, the wave structure between 82-85 km drifts against the wind, whereas a layer at 87 km between 05:20 and 05:30 UTC follows the background wind. Note the projected radial wind (from red to blue) indicating a westward wind. These events are good examples of the complicated dynamics within PMSE. Further analysis and interpretation of these high-resolution spatiotemporal structures will be done on a future work.

Figures 8 and 9 shows 3D maps of (a) the signal to noise ratio (SNR) (b) radial velocity, (c) locally enhanced SNR, and (d) residual radial velocity (i.e.,  $v_{res}$ ), for Events 1 and 2, respectively. In addition contours of locally enhanced SNR are overplotted on both the radial velocities. The SNR and radial velocity were obtained from the first and second spectral moments (e.g., Doviak and Zrnić, 1993). The locally enhanced SNR has been obtained using a 2D Gaussian function kernel with a width of 6 pixels. The local enhancements allow us to observe weak structures within strong one. For example, wave fronts are



distinguishable in Fig. 8c which were not visible in Fig. 8a. On the other hand, the residual radial velocity was estimated by removing the contributions of the estimated mean horizontal velocities in the measured radial velocities, i.e.,

$$v_{res}(\theta_x, \theta_y, \theta_z) = v_{rad}(\theta_x, \theta_y, \theta_z) - (u_0 \cdot \theta_x + v_0 \cdot \theta_y) \quad (8)$$

Assuming that the  $v_{res}$  is mainly due to the vertical motion, we can clearly see in Fig. 8d how up (red) and down (blue) structures drift across the illuminated area, maybe due to KHI. Similarly, Fig. 9 shows animated images of Event 2. In this case, the horizontal wind was small and most of the radial velocity was due to the vertical motion, i.e., radial velocity and residual velocities are almost the same. As mentioned above, in this event, the waves propagate horizontally against the weak horizontal wind.

The animated versions of Figs. 8 and 9 are shown in the supplemental material Movies S3 and S4, respectively. Although the information might be redundant when compared to Movies S1 and S2, we have decided to include them to provide a more standard view of typical spectral parameters of a multi-beam radar.

Making a quantitative comparison between SIMO and MIMO for real targets is not an easy task. We need a prior knowledge of the brightness to make a good analysis. This is not the case for PMSE. Fortunately, our observations include echoes from specular meteors and they can be used to evaluate quantitatively the angular resolution that can be achieved with our implementations. A specular meteor echo could be considered as a point target in angle. Along with its trajectory, the trail is long (hundreds of meters to a few kilometers) but its angular response is narrow. In the transverse direction to the trail, it is very narrow and its angular response is also narrow.

In Fig. 10 we show the normalized angular scattered power distribution for a specular meteor using SIMO and MIMO in combination with Capon and MaxEnt. As expected, the range resolution does not change for SIMO or MIMO [see Fig. 10(a)]. We see a peak at 89.1km and low power at other ranges. However, when comparing Capon and MaxEnt, MaxEnt shows us a clean power distribution along the whole ranges while Capon shows us a remaining sidelobe contamination at other ranges, coming from other angles. This indicates that, even with MIMO, Capon does not suppress the sidelobes as well as MaxEnt. Figures 10b and 10c show us the angular power distribution for  $\theta_x$  and  $\theta_y$  respectively, where the points are the samples for a given angle and the continuous line is a fitted Gaussian function. Using the fitted function we estimated the half power beam width (HPBW) for each implementation. Table 2 summarizes the angular resolution and the improvement factor for each method compared to the theoretical angular resolution of the full array MAARSY radar. As we expected the improvement between SIMO and MIMO is about 1.5 given that we increased the antenna aperture for MIMO by  $\sim 50\%$ . When combining MIMO and MaxEnt, surprisingly, we got an angular resolution of  $\sim 0.6^\circ$ , i.e., more than 5 times better than MAARSY's HPBW.

## 5 Discussion

We have shown qualitatively and quantitatively that radar imaging of PMSE is significantly improved by using MIMO instead of SIMO configurations, by at least 50%. Two different imaging methods have been applied, Capon and MaxEnt. As expected



from previous works, MaxEnt images are better than Capon images, however, MaxEnt is computationally more demanding. Similarly, we found that the quality of MIMO-Capon is comparable to SIMO-MaxEnt.

The preliminary results using MIMO-MaxEnt are allowing us to observe PMSE with unprecedented horizontal resolution (less than 1 km) compared to multibeam scanning experiments (Stober et al., 2013), and therefore the identification of structures with horizontal wavelengths less than 10 km (e.g., Event 1 above). For structures with wavelengths of the order of 15-20 km or so, the other imaging implementations, i.e., SIMO-Capon, SIMO-MaxEnt, MIMO-Capon, are sufficiently good to characterize them. These new capabilities will allow to better identify and characterize KHs and general GWs (not only monochromatic) than previously done at polar mesospheric heights during the summer. Our proposed technique complements previous observations that have been performed at nighttime when the sky is clear using airglows and lidars (e.g., M., 2013; Hecht et al., 2000, 2007; Taylor et al., 2007).

We will leave the detailed analysis and interpretation of these events and other events observed with this new capability for a future effort. In the following paragraphs, we discuss the technical results and propose future improvements.

The improved resolution using MIMO results from the larger effective visibility aperture and the larger number of independent samples, as compared to a SIMO configuration, i.e., 125 m instead of 76 m, and 475 instead of 163, respectively. In addition, the MaxEnt approach allows an improvement at least a factor of two in angular resolution when is compared to Capon. The maximum number of horizontal blobs that could theoretically be estimated for each range, time, and “color” (i.e., frequency bin) would be 79 ( $=475/6$ ), where each blob is characterized by a two-dimensional Gaussian function with 6 parameters (e.g., Chau and Woodman, 2001). Another reason to improve MIMO results is the number of redundant visibility measurements. Although they do not provide additional information in terms of degrees of freedom, the redundancy helps to reduce the statistical uncertainties of such visibility samples. Recall in our MIMO implementation, there are 1980 visibility samples ( $45 \times 44$ ) and only 475 are independent.

Despite the significant improvement, not everything is positive about applying MIMO. In the following paragraphs, we discussed the critical points of applying MIMO in terms of (a) power-aperture reduction, and (b) computational demands and real-time applicability.

As indicated by Urco et al. (2018), in atmospheric radars MIMO is applicable to targets with a large RCS, since a reduction of power-aperture is inherent to MIMO. In our particular application to PMSE, the transmitter sections were 1/7th of the total area, and therefore also 1/7th of the total transmitter power, i.e., -17 dB transmitting signal than usual experiments. In reception, 15 groups of 7 antennas (Hexagons) were used instead of the 433 available antennas. Moreover, given the time multiplexing, the number of coherent integrations was reduced and therefore the noise was increased, when compared to standard operations. In total, the sensitivity of our MIMO experiment is 27 dB less. Looking at the PMSE RCS in figure 2 of Latteck and Strelnikova (2015), our MIMO observations are limited to PMSE with RCS larger than  $10^{-14} \text{ m}^{-1}$ , i.e., approximately 40% of the usual seasonal MAARSY PMSE observations.

MaxEnt is known to be computationally more demanding than Capon in SIMO applications (e.g., Yu et al., 2001). In the case of MIMO, the computational demands are significantly increased given the larger number of effective receivers, i. e., 45 instead of 15. In terms of visibility pairs, the increase is from 210 to 1980! In the case of Capon, real-time processing is still



possible with these increased numbers of samples, however, MaxEnt for both SIMO and MIMO is not applicable in a real-time application. For example, for 80 seconds of data using an i5 PC with 15 cores, the processing times are 20 min and 3 hours for SIMO-MaxEnt and MIMO-MaxEnt, respectively. A future improvement to make MIMO-MaxEnt faster would be to use only one value of each redundant visibility sample, i.e., to work only with 475 independent samples instead of all 1980 measured visibility samples. Such value could be obtained either from the average of all the values sampling the same visibility or pre-selecting only one of them. After all, many of the independent samples are obtained with only one sample (green dots in Fig. 1e).

In general, a critical point for PMSE imaging is the drifting nature of the echoes. PMSE correlation times are relatively short, and under stationary conditions, one would require a few minutes of incoherent integration to reduce the statistical uncertainties of the visibility estimates. However, the structures to image would move between 2 and 5 km in 60 seconds for typical mesospheric motions (40-80 m/s), either from drifting with the background wind (Event 1) or from wave propagation (Event 2). These drifting structures limit further the angular resolution that can be accomplished by any method since the resulting image will be significantly blurred for integration times of a few minutes.

To deal with the drifting nature of PMSEs, in future studies we will explore tracking techniques, i.e., make use of this information to improve the angular resolution (e.g., Vaswani and Zhan, 2016). Given the computational demands of MaxEnt in particular when combined with MIMO, we will also explore radar imaging with compressed sensing (CS) techniques (e.g., Donoho, 2006; Candes and Wakin, 2008). Harding and Milla (2013) applied CS to Jicamarca F region irregularities, and show that CS produces results similar to MaxEnt. Our plan is to use MIMO-MaxEnt as a reference to other radar imaging techniques using SIMO, for example, CS in combination with tracking. Besides the computational demands, MIMO might not be applicable at other atmospheric radar sites, and therefore the exploration of other techniques using SIMO is required.

An additional improvement to the current observations would be the use of shorter pulses and therefore better range resolution, for example, 150 meters. Further improvement in range could be accomplished also by applying range imaging (e.g., Palmer et al., 1998; Yu and Palmer, 2001), particularly in combination with the radar imaging implementations of this work, allowing angular resolutions less than  $1^\circ$ .

## 25 6 Conclusions

In this work, we have successfully implemented coherent MIMO with radar imaging at MAARSY to observe PMSEs with unprecedented angular resolution. The obtained resolution results from the combination of a larger effective aperture, higher number of independent visibility samples resulting from MIMO, and improved angular resolution resulting from MaxEnt. Quantitatively, the maximum angular resolution accomplished is  $\sim 0.6^\circ$ , which is equivalent to having a 450-m diameter visibility aperture at 53.5 MHz and significant improvement to the MAARSY standard angular resolution of  $3.6^\circ$ .

The preliminary results with MIMO-MaxEnt allowed to clearly identify structures slightly less than 1 kilometer in diameter and wave-like structures with horizontal wavelengths less than 10 km, with a time resolution around 60 seconds. The identification of such structures with varying degrees of intensity, suggests that one has to be careful about using PMSE for estimating



the background wind assuming horizontal homogeneity. Not only the vertical wind is not homogeneous, but also the brightness is not homogeneous horizontally.

Given the relatively long temporal correlation of PMSEs, i.e., a few minutes, larger integration in time of the noisy visibility would allow less statistical uncertainties in the resulting images of the two events presented. However, PMSE structures drift as they are imaged, therefore long integration times result in angular smearing. In the future, we plan to use the drifting information to improve the angular resolution, by applying tracking techniques.

As mentioned above, the implementation of MIMO-MaxEnt is computationally intensive and is currently not applicable to real-time processing. On the other hand, MIMO-Capon can be implemented in real-time processing. Our strategy for near future observations would be to use MIMO-Capon for real-time processing and on special events use MIMO-MaxEnt until more efficient implementations and/or faster computers are available.

*Competing interests.* TEXT

*Acknowledgements.* We would like to thank Toralf Renkwitz for providing the receivers' phase offsets and Marius Zecha for MAARSY data handling. This work was partially supported by the Deutsche Forschungsgemeinschaft (DFG, German Research Foundation) under SPP 1788 (CoSIP)-CH1482/3-1 and by the WATILA Project (SAW-2015-IAP-1).



## References

- Balsley, B. B. and Riddle, A. C.: Monthly mean values of the mesospheric wind field over Poker Flat, Alaska, *Journal of the Atmospheric Sciences*, 41, 2368–2375, 1984.
- Baumgarten, G. and Fritts, D. C.: Quantifying Kelvin-Helmholtz instability dynamics observed in noctilucent clouds: 1. Methods and observations, *Journal of Geophysical Research: Atmospheres*, 119, 9324–9337, <https://doi.org/10.1002/2014JD021832>, <http://dx.doi.org/10.1002/2014JD021832>, 2014JD021832, 2014.
- Candes, E. J. and Wakin, M. B.: An introduction to compressive sampling, *IEEE Signal Processing Magazine*, 25, 21–30, <https://doi.org/10.1109/MSP.2007.914731>, 2008.
- Capon, J.: High-resolution frequency-wavenumber spectrum analysis, *Proc. IEEE*, 57, 1408–1419, 1969.
- 10 Chau, J. L. and Woodman, R. F.: Three-dimensional coherent radar imaging at Jicamarca: Comparison of different inversion techniques, *J. Atmos. Sol. Terr. Phys.*, 63, 253–261, 2001.
- Chau, J. L., Renkowitz, T., Stober, G., and Latteck, R.: MAARSY multiple receiver phase calibration using radio sources, *Journal of Atmospheric and Solar-Terrestrial Physics*, 118, 55–63, 2014.
- Chau, J. L., Stober, G., Hall, C. M., Tsutsumi, M., Laskar, F. I., and Hoffmann, P.: Polar mesospheric horizontal divergence and relative vorticity measurements using multiple specular meteor n/a–n/a, <https://doi.org/10.1002/2016RS006225>, <http://dx.doi.org/10.1002/2016RS006225>, 2016RS006225, 2017.
- 15 Chau, J. L., McKay, D., Vierinen, J. P., La Hoz, C., Ulich, T., Lehtinen, M., and Latteck, R.: Multi-static spatial and angular studies of polar mesospheric summer echoes combining MAARSY and KAIRA, *Atmospheric Chemistry and Physics*, 18, 9547–9560, <https://doi.org/10.5194/acp-18-9547-2018>, <https://www.atmos-chem-phys.net/18/9547/2018/>, 2018.
- 20 Czechowsky, P., Reid, I. M., and Rüster, R.: VHF radar measurements of the aspect sensitivity of the summer polar mesopause echoes over Andenes (69°N,16°E), Norway, *Geophysical Research Letters*, 15, 1259–1262, <https://doi.org/10.1029/GL015i011p01259>, <http://dx.doi.org/10.1029/GL015i011p01259>, 1988.
- Donoho, D. L.: Compressed sensing, *IEEE Transactions on Information Theory*, 52, 1289–1306, <https://doi.org/10.1109/TIT.2006.871582>, 2006.
- 25 Doviak, R. J. and Zrnić, D. S.: Weather signal processing, in: *Doppler radar and weather observations*, pp. 122 – 159, Academic Press, second edition edn., <https://doi.org/https://doi.org/10.1016/B978-0-12-221422-6.50011-5>, 1993.
- Ecklund, W. L. and Balsley, B. B.: Long-term observations of the Arctic mesosphere with the MST radar at Poker Flat, Alaska, *J. Geophys. Res.*, 86, 1981.
- Foschini, G. J. and Gans, M. J.: On limits of wireless communications in a fading environment when using multiple antennas, *Wireless*
- 30 *Personal Communications*, 6, 311–335, 1998.
- Fritts, D. C., Tsuda, T., VanZandt, T. E., Smith, S. A., Sato, T., Fukao, S., and Kato, S.: Studies of velocity fluctuations in the lower atmosphere using the MU radar. Part II: Momentum fluxes and energy densities, *J. Atmos. Sci.*, 47, 51–66, 1990.
- Harding, B. J. and Milla, M.: Radar imaging with compressed sensing, *Radio Science*, 48, 582–588, 2013.
- Havnes, O., Trøim, J., Blix, T., Mortensen, W., Naesheim, L. I., Thrane, E., and Tønnesen, T.: First detection of charged dust particles
- 35 in the Earth’s mesosphere, *Journal of Geophysical Research: Space Physics*, 101, 10 839–10 847, <https://doi.org/10.1029/96JA00003>, <https://agupubs.onlinelibrary.wiley.com/doi/abs/10.1029/96JA00003>, 1996.



- Hecht, J. H., Fricke-Begemann, C., L., W. R., and Höffner, J.: Observations of the breakdown of an atmospheric gravity wave near the cold summer mesopause at 54N, *Geophys. Res. Lett.*, 27, 879–882, 2000.
- Hecht, J. H., Liu, A. Z., Walterscheid, R. L., Franke, S. J., Rudy, R. J., Taylor, M. J., and Pautet, P.-D.: Characteristics of short- period wavelike features near 87 km altitude from airglow and lidar observations over Maui, *Geophys. Res. Atmos.*, 112, 2007.
- 5 Hoppe, U., Hall, C., and Röttger, J.: First observations of summer polar mesospheric backscatter with a 224 MHz radar, *Geophysical Research Letters*, 15, 28–31, <https://doi.org/10.1029/GL015i001p00028>, <https://agupubs.onlinelibrary.wiley.com/doi/abs/10.1029/GL015i001p00028>, 1988.
- Hoppe, U.-P. and Fritts, D. C.: High-resolution measurements of vertical velocity with the European incoherent scatter VHF radar: 1. Motion field characteristics and measurement biases, *Journal of Geophysical Research: Atmospheres*, 100, 16 813–16 825, 1995.
- 10 Hoppe, U.-P., Fritts, D., Reid, I., Czechowsky, P., Hall, C., and Hansen, T.: Multiple-frequency studies of the high-latitude summer mesosphere : implications for scattering processes, *Journal of Atmospheric and Terrestrial Physics*, 52, 907 – 926, [https://doi.org/https://doi.org/10.1016/0021-9169\(90\)90024-H](https://doi.org/https://doi.org/10.1016/0021-9169(90)90024-H), <http://www.sciencedirect.com/science/article/pii/002191699090024H>, middle atmosphere dynamics at high latitudes, 1990.
- Huang, Y., Brennan, P. V., Patrick, D., Weller, I., Roberts, P., and Hughes, K.: FMCW based MIMO imaging radar for maritime navigation, *Progress In Electromagnetics Research*, 115, 327–342, 2011.
- 15 Hysell, D. L.: Radar imaging of equatorial *F* region irregularities with maximum entropy interferometry, *Radio Sci.*, 31, 1567–1578, 1996.
- Hysell, D. L. and Chau, J.: Optimal aperture synthesis radar imaging, *Radio Sci.*, 41, 2006.
- Kaifler, N., Baumgarten, G., Fiedler, J., Latteck, R., Lübken, F.-J., and Rapp, M.: Coincident measurements of PMSE and NLC above ALO-MAR (69°N, 16°E) by radar and lidar from 1999–2008, *Atmospheric Chemistry and Physics*, 11, 1355–1366, [https://doi.org/10.5194/acp-](https://doi.org/10.5194/acp-11-1355-2011)
- 20 [11-1355-2011](https://doi.org/10.5194/acp-11-1355-2011), <https://www.atmos-chem-phys.net/11/1355/2011/>, 2011.
- Kelley, M. C. and Ulwick, J. C.: Large- and small-scale organization of electrons in the high-latitude mesosphere: Implications of the STATE data, *Journal of Geophysical Research: Atmospheres*, 93, 7001–7008, <https://doi.org/10.1029/JD093iD06p07001>, <https://agupubs.onlinelibrary.wiley.com/doi/abs/10.1029/JD093iD06p07001>, 1988.
- Kudeki, E. and Sürücü, F.: Radar interferometric imaging of field-aligned plasma irregularities in the Equatorial Electrojet, *Geophys. Res. Lett.*, 18, 41–44, 1991.
- 25 Latteck, R. and Strelnikova, I.: Extended observations of polar mesosphere winter echoes over Andøya (69°N) using MAARSY, *Journal of Geophysical Research: Atmospheres*, 120, 8216–8226, <https://doi.org/10.1002/2015JD023291>, <http://dx.doi.org/10.1002/2015JD023291>, 2015JD023291, 2015.
- Latteck, R., Singer, W., Rapp, M., Renkowitz, T., and Stober, G.: Horizontally resolved structures of radar backscatter from polar mesospheric layers, *Adv. Radio Sci.*, 10, 1–6, 2012a.
- 30 Latteck, R., Singer, W., Rapp, M., Vandeppeer, B., Renkowitz, T., Zecha, M., and Stober, G.: MAARSY: The new MST radar on Andøya – System description and first results, *Radio Sci.*, 47, RS1006, 2012b.
- M., S. S.: The identification of mesospheric frontal gravity-wave events at a mid-latitude site, *Adv. Space Res.*, 10, 1016, 2013.
- Palmer, R. D., Gopalam, S., Yu, T. Y., and Fukao, S.: Coherent radar imaging using Capon’s method, *Radio Sci.*, 33, 1585–1598, 1998.
- 35 Rapp, M. and Lübken, F.-J.: Polar mesosphere summer echoes (PMSE): Review of observations and current understanding, *Atmospheric Chemistry and Physics*, 4, 2601, 2004.
- Rapp, M., Gumbel, J., Lübken, F.-J., and Latteck, R.: D region electron number density limits for the existence of polar mesosphere summer echoes, *Journal of Geophysical Research (Atmospheres)*, 107, 4187, 2002.



- Sommer, S. and Chau, J. L.: Patches of polar mesospheric summer echoes characterized from radar imaging observations with MAARSY, *Annales Geophysicae*, 34, 1231–1241, <https://doi.org/10.5194/angeo-34-1231-2016>, 2016.
- Stebel, K., Barabash, V., Kirkwood, S., Siebert, J., and Fricke, K. H.: Polar mesosphere summer echoes and noctilucent clouds: Simultaneous and common-volume observations by radar, lidar and CCD camera, *Geophysical Research Letters*, 27, 661–664, <https://doi.org/10.1029/1999GL010844>, <https://agupubs.onlinelibrary.wiley.com/doi/abs/10.1029/1999GL010844>, 2000.
- 5 Stober, G., Sommer, S., Rapp, M., and Latteck, R.: Investigation of gravity waves using horizontally resolved radial velocity measurements, *Atmospheric Measurement Techniques*, 6, 2893–2905, 2013.
- Stober, G., Sommer, S., Schult, C., Latteck, R., and Chau, J. L.: Observation of Kelvin–Helmholtz instabilities and gravity waves in the summer mesopause above Andenes in Northern Norway, *Atmospheric Chemistry and Physics*, 18, 6721–6732, <https://doi.org/10.5194/acp-18-6721-2018>, <https://www.atmos-chem-phys.net/18/6721/2018/>, 2018.
- 10 Taylor, M. J., Pendleton Jr, W. R., Pautet, P.-D., Zhao, Y., Olsen, C., Babu, H. K. S., Medeiros, A. F., and Takahashi, H.: Recent progress in mesospheric gravity wave studies using night-glow imaging system, *Geophys. Res. Lett.*, 25, 49–58, 2007.
- Telatar, E.: Capacity of multi-antenna Gaussian channels, *European Transactions on Telecommunications*, 10, 585–595, <https://doi.org/10.1002/ett.4460100604>, <http://dx.doi.org/10.1002/ett.4460100604>, 1999.
- 15 Urco, J. M., Chau, J. L., Milla, M. A., Vierinen, J. P., and Weber, T.: Coherent MIMO to improve aperture synthesis radar imaging of field-aligned irregularities: First results at Jicamarca, *IEEE Transactions on Geoscience and Remote Sensing*, 56, 2980–2990, <https://doi.org/10.1109/TGRS.2017.2788425>, 2018.
- Varney, R. H., Kelley, M. C., Nicolls, M. J., Heinselman, C. J., and Collins, R. L.: The electron density dependence of polar mesospheric summer echoes, *J. Atmos. Sol. Terr. Phys.*, 73, 2153–2165, 2011.
- 20 Vaswani, N. and Zhan, J.: Recursive recovery of sparse signal sequences from compressive measurements: A review, *IEEE Transactions on Signal Processing*, 64, 3523–3549, <https://doi.org/10.1109/TSP.2016.2539138>, 2016.
- Woodman, R. F.: Coherent radar imaging: Signal processing and statistical properties, *Radio Sci.*, 32, 2373–2391, 1997.
- Woodman, R. F. and Chau, J. L.: Antenna compression using binary phase coding, *Radio Sci.*, 36, 45–52, 2001.
- Yu, T.-Y. and Palmer, R. D.: Atmospheric radar imaging using multiple-receiver and multiple-frequency techniques, *Radio Science*, 36, 1493–1503, <https://doi.org/10.1029/2000RS002622>, <https://agupubs.onlinelibrary.wiley.com/doi/abs/10.1029/2000RS002622>, 2001.
- 25 Yu, T.-Y., Palmer, R. D., and Chilson, P. B.: An investigation of scattering mechanisms and dynamics in PMSE using coherent radar imaging, *Journal of Atmospheric and Solar-Terrestrial Physics*, 63, 1797 – 1810, [https://doi.org/https://doi.org/10.1016/S1364-6826\(01\)00058-X](https://doi.org/https://doi.org/10.1016/S1364-6826(01)00058-X), <http://www.sciencedirect.com/science/article/pii/S136468260100058X>, 2001.
- Zecha, M., Röttger, J., Singer, W., Hoffmann, P., and Keuer, D.: Scattering properties of PMSE irregularities and refinement of velocity estimates, *Journal of Atmospheric and Solar-Terrestrial Physics*, 63, 201–214, 2001.
- 30

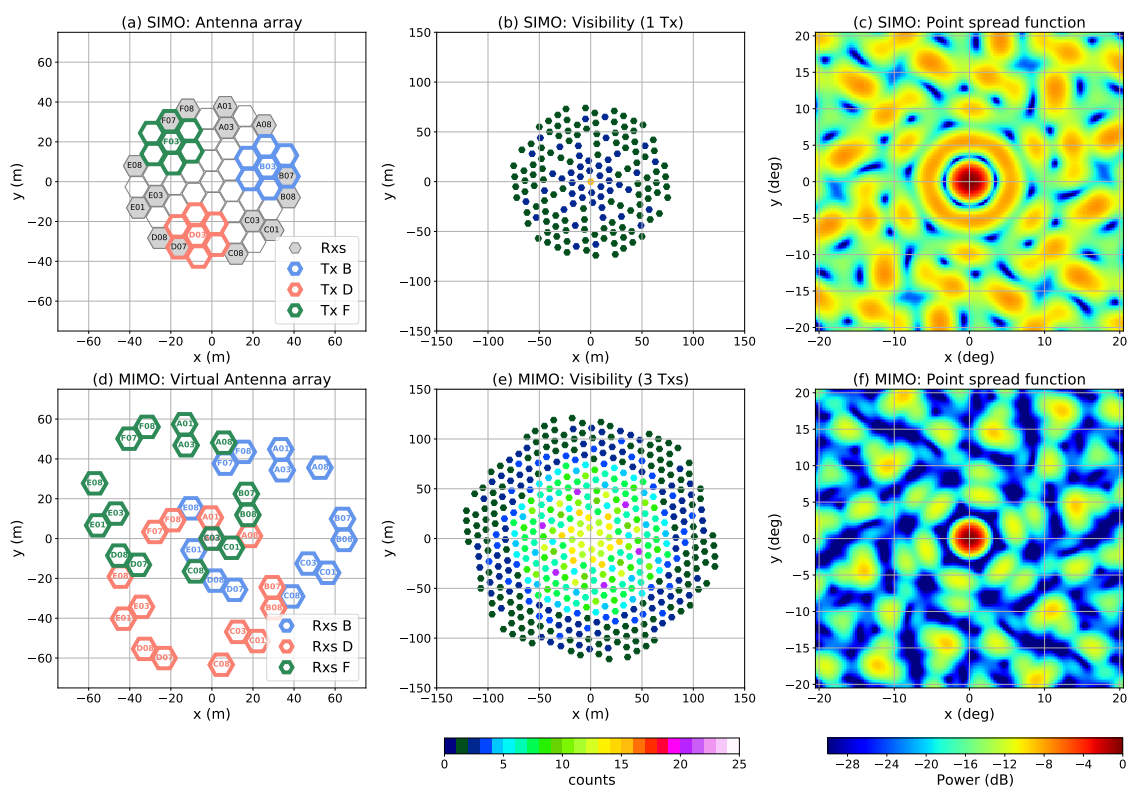


**Figure 1.** MAARSY antenna configuration for SIMO (top) and MIMO (bottom): Anemones and hexagons used for transmission and reception, respectively (first column); visibility samples (second column), and point-spread (or instrument) function. In the case of MIMO, (d) shows the virtual position of the resulting receiving antennas. See text for further details.

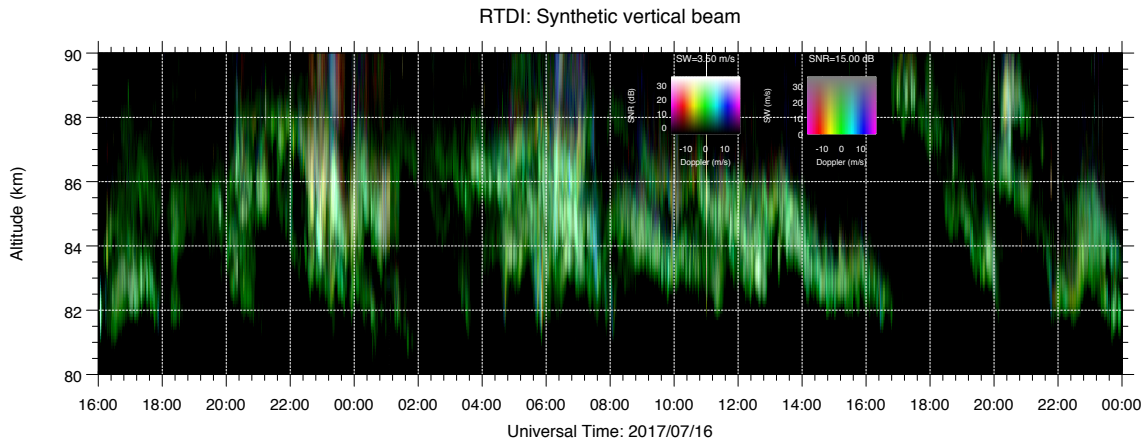


**Figure 2.** A 24-bit image of range-time Doppler intensity (RTDI) plot of PMSE using MIMO with time diversity conducted on July 16 and 17, 2017. The signal intensity is represented as lightness, Doppler information as hue, and spectral width as saturation. The legend on the left represent the SNR vs Doppler color map for a saturation of 90%. The legend on the right represents the spectral width vs Doppler for a lightness of 50%. Note that only the signal corresponding to the narrow region in the illuminated area is shown.

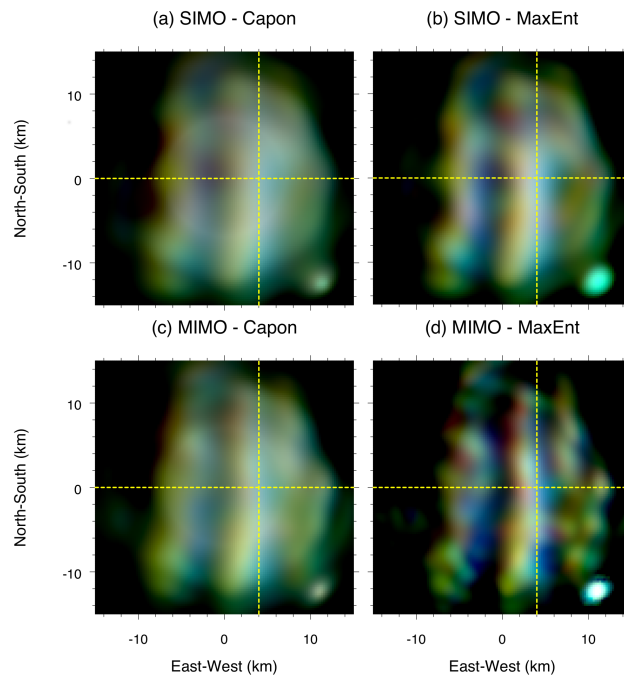


**Figure 3.** EW-NS images for  $z=85.8$  km obtained from applying four different implementation (a) SIMO-Capon, (b) SIMO-MaxEnt, (c) MIMO-Capon, (d) MIMO-MaxEnt, at 00:56:55 UT on July 17, 2017, i.e., Event 1. Images are color coded as same as Figure 2. The yellow dashed horizontal/vertical lines represent the location of the NS/EW cuts shown in later figures for Event 1.

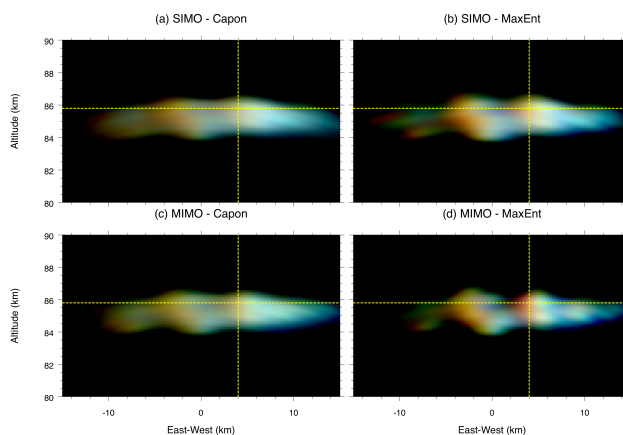


**Figure 4.** Similar to Fig. 3, but for an EW-Altitude cut at  $y=0$  km. The yellow dashed horizontal lines represent the location of the altitude cuts shown in previous and later figures for Event 1.

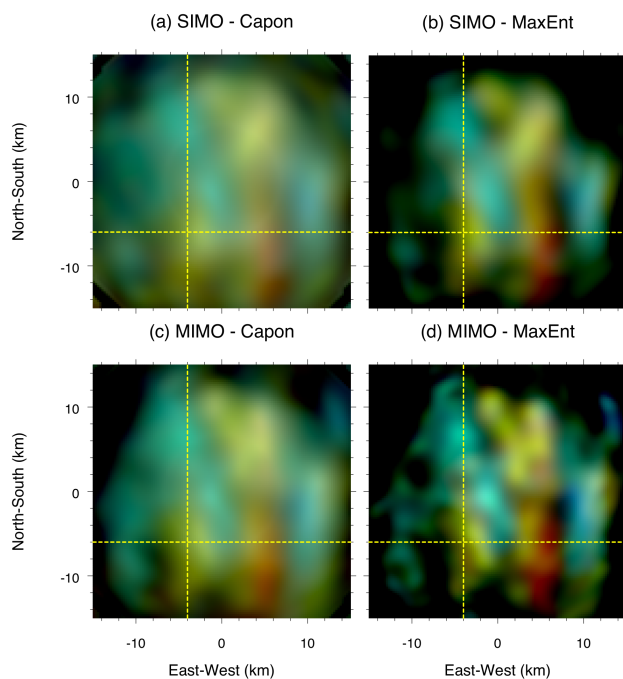


**Figure 5.** Same as Figure 3 but at 05:56:13 UT on July, 2017, i.e., Event 2. The yellow dashed horizontal/vertical lines represent the location of the NS/EW cuts shown in later figures for Event 2.

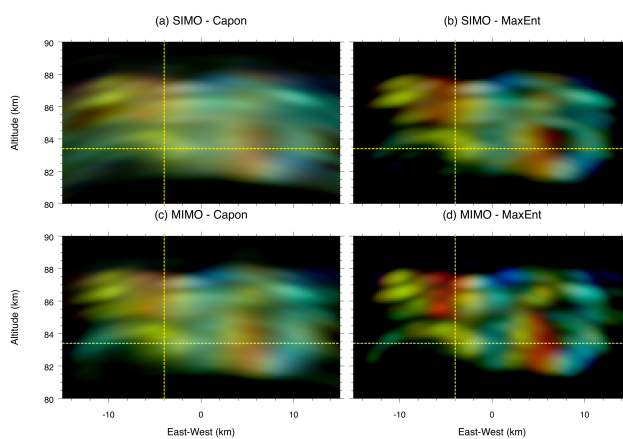


**Figure 6.** Same as Figure 5 but for an EW-Altitude cut at  $y=-6$  km. The yellow dashed horizontal lines represent the location of the altitude cuts shown in previous and later figures for Event 2.

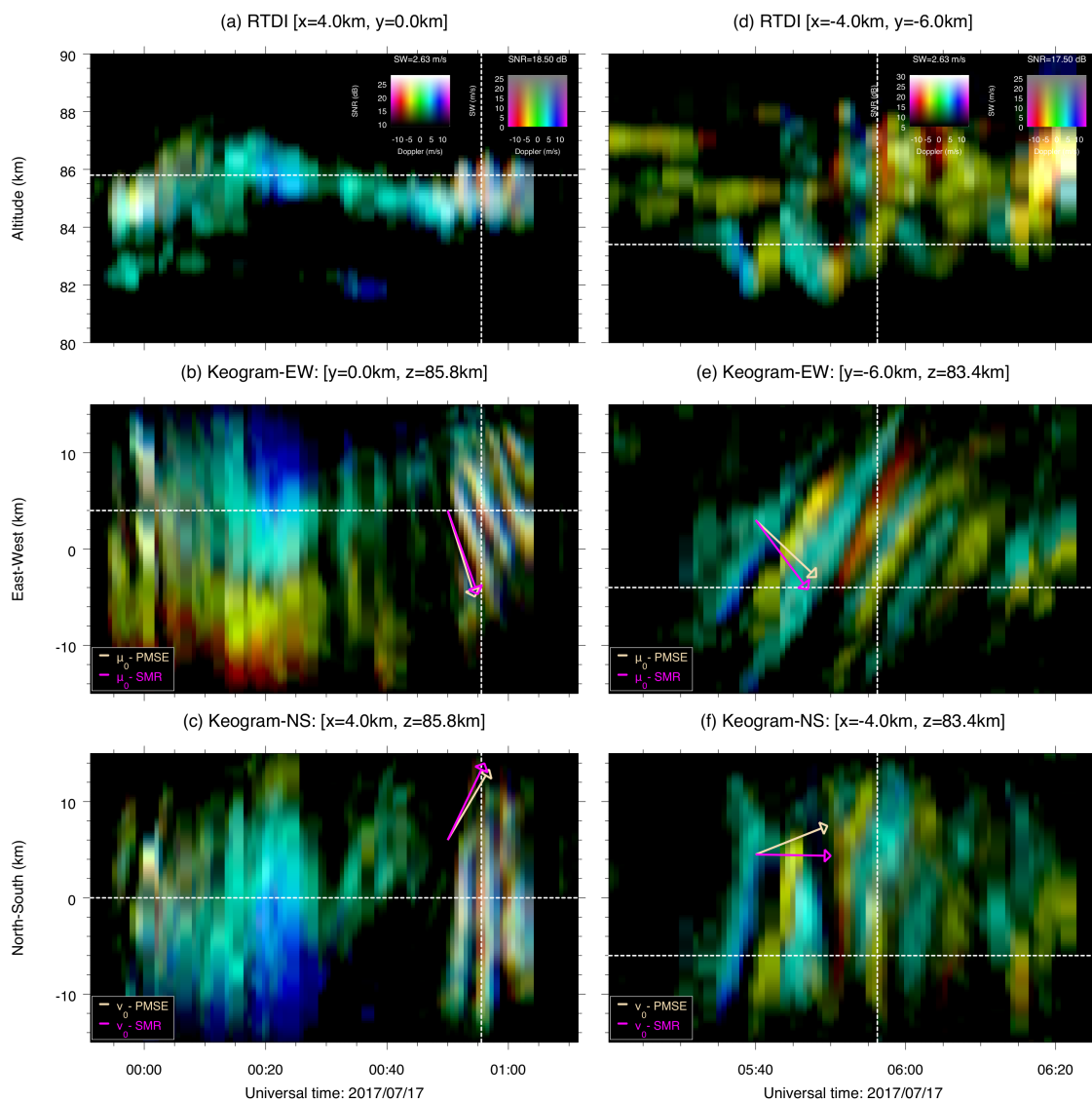


**Figure 7.** 24-bit time representation images of PMSE structures as function of: altitude (RTDI) (first row), EW location (Keogram) (second row), and NS location (Keogram) (third row) for selected cuts, for both Event 1 (first column) and Event 2 (second column). In the keograms, the wind components obtained with specular meteor radars (SMRs) and MAARSY PMSE are shown with pink and yellow arrows, respectively. The white dashed horizontal lines represent the location of the altitude, EW and NS cuts shown in previous figures and current keograms for Event 1 and 2. The white dashed vertical lines represent the time of the cuts shown in previous figures.

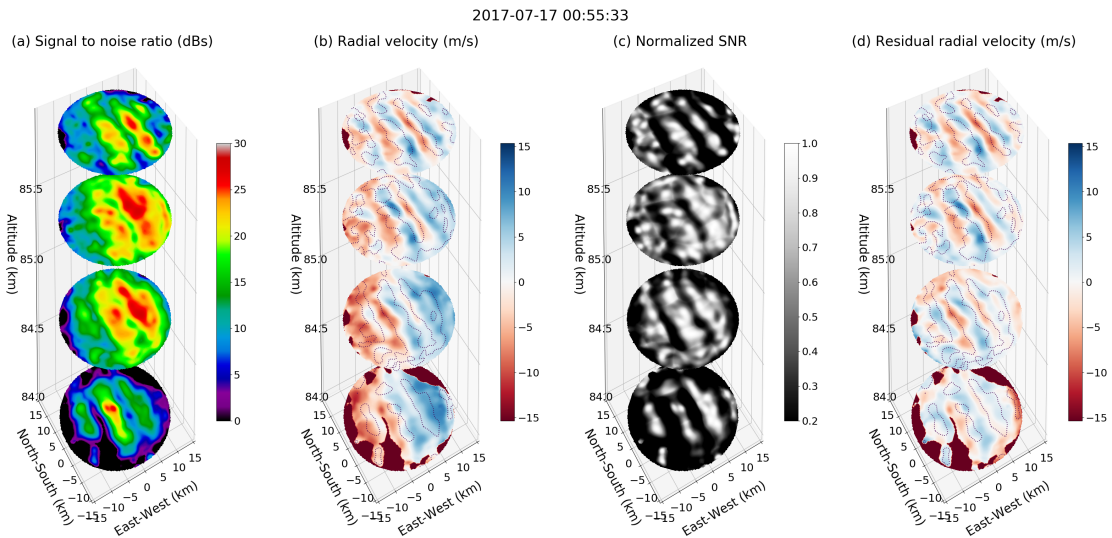


**Figure 8.** Three-dimensional contour plots at 00:55:33 UT on July 17, 2017, i.e., Event 1, for four selected altitudes : 84km, 84.6km, 85.2km, and 85.8km. For each altitude is shown: (a) SNR, (b) radial velocity, (c) Locally enhanced SNR, and (d) residual radial velocity. Contour on locally enhanced SNR are overlotted in both velocity plots.

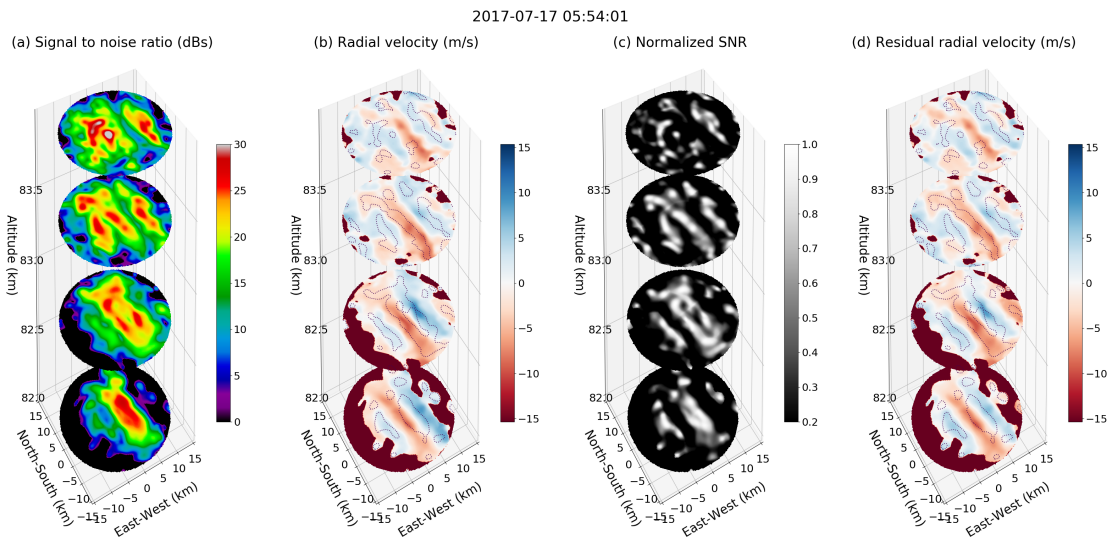


**Figure 9.** Same as 8, but at 05:54:01 on July 17, 2017 for altitudes: 82km, 82.7km, 83.4km, and 84km., i.e., Event 2.

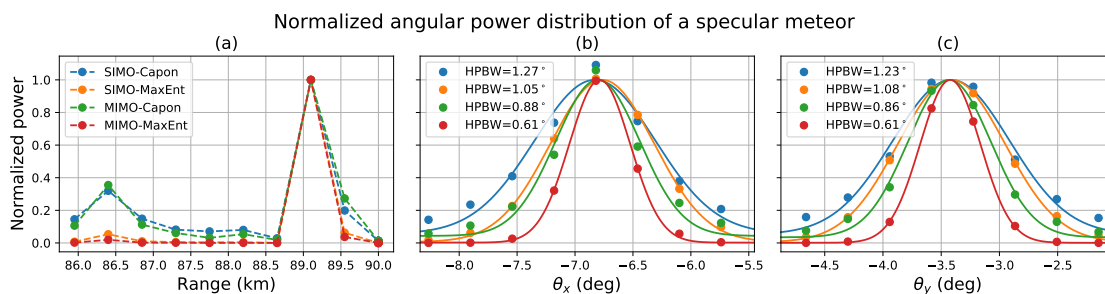


**Figure 10.** Normalized angular power distribution of a specular meteor echo as function of: (a) range, (b) EW angle ( $\theta_x$ ), and NS angle ( $\theta_y$ ). The results are shown for all four implementations, i.e., SIMO-Capon (blue), SIMO-MaxEnt (orange), MIMO-Capon (green), and MIMO-MaxEnt (red).



**Table 1.** Parameters of MAARSY MIMO experiment

Parameter	Value
Frequency	53.5MHz
Pulse repetition frequency (PRF)	1000Hz
Pulse coding	Complementary 16
Number of transmitters (beams)	5
Transmit diversity	Time
Tx interleaving	2ms
Number of coherent integrations	8
Effective PRF (after integration)	25Hz
Number of FFT points	16
Number of incoherent integrations	128
Equivalent integration time	81.92s
Range resolution	450m

**Table 2.** Performance of imaging techniques

Technique	Angular resolution	Spatial resolution at 85km	Equivalent antenna aperture	Improvement factor
MAARSY	3.60°	5.33km	76m	1.00
SIMO - Capon	1.27°	1.88km	216m	2.83
MIMO - Capon	0.88°	1.30km	312m	4.09
SIMO - MaxEnt	1.05°	1.55km	261m	3.42
MIMO - MaxEnt	0.61°	0.90km	450m	5.90